Bernardi et al. *EPJ Quantum Technology* (2020) 7:13
https://doi.org/10.1140/epjqt/s40507-020-00088-2

EPJ Quantum Technology
a SpringerOpen Journal

RESEARCH Open Access

A biocompatible technique for magnetic field sensing at (sub)cellular scale using Nitrogen-Vacancy centers

Ettore Bernardi[1*], Ekaterina Moreva[1], Paolo Traina[1], Giulia Petrini[1,2], Sviatoslav Ditalia Tchernij[2], Jacopo Forneris[2,3], Željko Pastuović[4], Ivo Pietro Degiovanni[1], Paolo Olivero[2,3] and Marco Genovese[1]

*Correspondence:
e.bernardi@inrim.it
[1]Istituto Nazionale di Ricerca Metrologica, Strada delle cacce 91, Turin, Italy
Full list of author information is available at the end of the article

Abstract

We present an innovative experimental set-up that uses Nitrogen-Vacancy centres in diamonds to measure magnetic fields with the sensitivity of $\eta = 68 \pm 3\ \mathrm{nT}/\sqrt{\mathrm{Hz}}$ at demonstrated (sub)cellular scale. The presented method of magnetic sensing, utilizing a lock-in based ODMR technique for the optical detection of microwave-driven spin resonances induced in NV centers, is characterized by the excellent magnetic sensitivity at such small scale and the full biocompatibility. The cellular scale is obtained using a NV-rich sensing layer of 15 nm thickness along *z* axis and a focused laser spot of $(10 \times 10)\ \mu\mathrm{m}^2$ in *x*-*y* plane. The biocompatibility derives from an accurate choice of the applied optical power. For this regard, we also report how the magnetic sensitivity changes for different applied laser power and discuss the limits of the sensitivity sustainable with biosystem at such small volume scale. As such, this method offers a whole range of research possibilities for biosciences.

Keywords: NV centers; Quantum sensing; Magnetic measurements

1 Introduction

Magnetometry in biological systems is of the utmost importance for fundamental biological science and medicine [1]. Mapping brain activity by recording magnetic fields produced by the electrical currents which are naturally occurring in the brain is of extreme interest [2, 3], with direct applications in the timely detection and cure of psychic and neurodegenerative disorders [4–6]. Measuring the magnetic fields produced by electrical currents in the heart is also of the utmost importance [7], since this could lead to a new generation of non-invasive diagnostic and therapeutic techniques [8]. Superconductive quantum interference device (SQUID) magnetometers are usually used for both these kinds of measurements. Nonetheless, the significant drawbacks of SQUID magnetometers are represented by the facts that they are unable to sense single nerve pulses, and they are costly, bulky, and require cryogenic refrigeration [9, 10].

Magnetometers based on Nitrogen-Vacancy (NV) centers in diamond represent a valid alternative to SQUID-based magnetometry. Firstly, diamond offers the substantial advan-

tage of being fully biocompatible [6, 11–15]. On the other side, NV centers are characterized by a peculiar electronic level structure that allows the optical detection of their microwave-driven spin resonances with a technique referred as Optically Detected Magnetic Resonance(ODMR) [16–19]. The shift in the ODMR frequency is related to the projection of the local magnetic field along the NV center axis. If an ensemble of NV centers is used, it is possible to reconstruct the 3D structure of the field, taking advantage of the 4-different possible orientations of the NV axis within the surrounding crystal structure. [20].

NV magnetometry has already been exploited to detect the action potential in a macroscopic biological sample [21]. In this proof-of-principle experiment, Barry and coworkers achieved a magnetic field sensitivity of $\eta = 15 \pm 1$ pT/$\sqrt{\text{Hz}}$ with a sensing volume, i.e. the volume containing the ensemble of the excited centers, of $(13 \times 2000 \times 2000)$ μm^3 and optical power of 2.75–4.5 W. To extend NV-based-biomagnetometry from macroscopic samples to small tissues up to single cells, a smaller sensing volume and a lower optical power should be used. The characteristic size of a cell is approximately 10–40 μm, and the laser power used in confocal measurement on living cells reported in [22] is in the range of few mW.

In this work, we present a NV-magnetometry protocol characterized by a sensing volume of $(0.015 \times 10 \times 10)$ μm^3, i.e. much smaller than the sensing volume used for macroscopical biological samples, and optical powers from 2.5 mW to 80 mW, values compatible, as we will discuss, with magnetometry at the cellular level. Our set-up, being suitable for the *in-vitro* measurement of biological magnetic fields at the (sub)cellular scale on cultivated cells, paves the way to the experimental study of biological processes (such as the action potential generation) inside the cell.

2 Experimental

The ODMR technique is based on the fact that the application of a magnetic field removes the energy degeneracy between the $m_S = \pm 1$ spin states of a NV color center, since the frequency difference $\nu_+ - \nu_-$ between the two ODMR dips is proportional to the component B_{NV} of the field along the NV-axis:

$$\nu_+ - \nu_- = \frac{1}{h} 2 g \mu_B B_{\text{NV}} \tag{1}$$

(where g is the Landé factor and μ_B the Bohr magneton), a measurement of this shift directly detect the intensity of the applied field. Infact, A variation δB_{NV} in the applied magnetic field causes a shift $\delta\nu_+ = \frac{1}{h} g \mu_B \delta B_{\text{NV}}$ to the higher-frequency ODMR dip and a corresponding $\delta\nu_- = -\frac{1}{h} g \mu_B \delta B_{\text{NV}}$ shift for the lower-frequency one. Tracking the ODMR shift, $\delta\nu_+$ or $\delta\nu_-$, allows the measurement of the variation of the applied field δB_{NV}.

The simplest way to track the ODMR shift is to collect the photoluminscence signal while scanning the microwave frequency. Adopting a frequency modulation of the microwaves can improve this method: the modulating signal is centered at the resonance dip and has an amplitude equal to the full-width half maximum of the resonance [21, 23]. The resulting modulated photoluminescence signal is read by a lock-in amplifier(LIA), see Fig. 1. The resulting LIA signal is a linear function of ODMR shift. This technique has also the advantage to shift the spectrum of the signal in a region where the technical noise is lower.

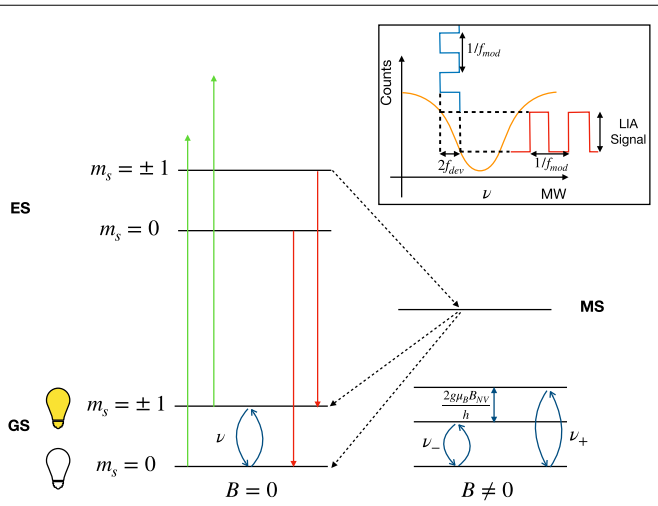

Figure 1 Main Figure: Schematics of the NV level scheme and of applied drivings. Green laser (green arrows) drives not-resonant optical spin-preserving transition from ground state(GS) to excited state(ES). Relaxation from ES to GS happens trough a radiative decay for states with $m_s = 0$, resulting in red photoluminescence (red-arrows). For the state with $m_s = \pm 1$ relaxation happens either trough a radiative decay as in the previous case and trough a not-radiative decay involving a metastable state (MS) (dashed black lines). These results in a higher photoluminesce (turn-on lamp) for state with $m_s = 0$ compared to state with $m_s = \pm 1$ (turn-off lamp). Populations of the spin staes can be varied by resonant microwave magnetic field (blue arrow) of frequency ν. A resonant magnetic field will increase the $m_s = \pm 1$ state population causing a decrease in red photoluminesce. The application of a magnetic field removes the energy degeneracy between the $m_S = \pm 1$ spin states, creating two separate resonance frequencies ν_- and ν_+. Inset: Schematics of lock-in detection. The microwave signal is frequency modulated with an ampltude $f_{\mathbf{dev}}$ at a frequency $f_{\mathbf{mod}}$. $f_{\mathbf{dev}}$, is equal to the full- width half maximum of the original ODMR signal. The resulting photoluminescence signal will be also modulated at frequency $f_{\mathbf{mod}}$

Figure 2 depicts the experimental set-up: the diamond sensor, laser excitation system, the microwave generation and LIA detection apparatus. The diamond sample was mounted on a microwave planar ring antenna, specifically designed for ODMR measurements in a 400 MHz frequencies range centered around the 2.87 GHz spin resonance [24].

The pristine sample was a $3 \times 3 \times 0.3$ mm^3 diamond substrate produced by ElementSix by CVD deposition. The sample was classified as an "optical grade" CDV diamond for having the nominal concentration of substitutional nitrogen and boron of < 1 ppm and 0.05 ppm, respectively. The sample was implanted with 10 keV N ions at room temperature using a low energy ion implanter. Implanted N ions fluence (dose) was 1×10^{14} cm^{-2}. Implanted sample was and subsequently annealed for 2 hours at temperature of 950C. This process resulted in the formation of NV centers in a $\sim 3 \cdot 10^{19}$ cm^{-3} concentration across a $\sim$15 nm thick layer at $\sim$10 nm from the sample surface, see inset of Fig. 2.

The excitation light (80 mW optical power) at 532 nm was obtained by the second harmonic of a Nd:YAG laser with high power stability (Coherent Prometheus 100NE) and was focused close to the bottom surface (i.e. the one incorporating the NV layer) of the diamond sample through an air objective (Olympus UPLANFL) with Numerical Aperture NA = 0.67. The diameter of the spot of the focused laser beam is $\sim(10 \times 10)$ μm^2. The power of the excitation light is varied using a Neutral Density filter. An Acousto Optic Modulator after the laser source is exploited to switch on and off the laser illumination on the sample. This solution allows to shine the laser on the sample only during the mea-

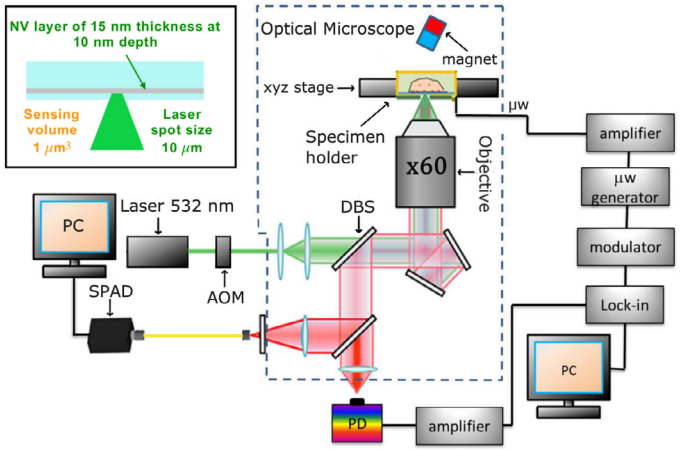

Figure 2 Schematics of the experimental set-up. The optical excitation using a green laser, the microwave(μw) control and the lock-in detection are depicted. The optical excitation is switch on and off using an Acousto Optic Modulator (AOM). The green laser beam is focused to a spot of $\sim(10 \times 10)\ \mu m^2$ size. A Dichroic Beam Splitter (DBS) is used to separate the optical path of the green excitation and of the red photoluminescence (PL). The 96% of the PL is then sent to a photodiode (PD), the remaining 4% is sent single-photon avalanche detector(SPAD). In the inset a drawing of the sample is shown. The sensing layer has a thickness of 15 nm and a is localized at depth of 10 nm below the surface

surement time, reducing the total amount of light energy delivered to the sample. This is of key importance in biological applications.

The microwave control was obtained by a commercial microwave generator (Keysight N5172B) whose central frequency was internally modulated at f_{mod} = 5001 Hz with modulation depth f_{dev} = 0.5 MHz, f_{dev} represents the deviation from the central microwave frequency, see inset in Fig. 1. For simultaneous hyperfine driving, the microwave was mixed via a double-balanced mixer with a $\sim$2.16 MHz sinewave to create two simultaneous driving modulated frequencies near the central frequency. Then, the microwave generator was connected to the LIA to provide a sinusoidal reference channel modulated at f_{mod}.

A permanent magnet fixed on a translation stage, allowing micrometric movement along the three spatial axes, provided the external magnetic field applied to the diamond sample.

The photoluminescence (PL) emission was spectrally filtered with a notch filter centered at 532 nm and a long-pass filter centered at 650 nm, then collected and detected with two different acquisition systems. A 4% fraction of the total PL intensity was sent to a single-photon avalanche detector (SPAD). The signal from the SPAD was used for the ODMR spectrum acquisition. The remaining 96% fraction of the emitted PL intensity was collected by NA = 0.25 objective (Olympus 10×) and imaged onto a photodetector (Thorlabs DET 10A2). Finally, the signal from the photodiode was sent to the input channel of the LIA.

In the measurement of the Linear Spectral Density(LSD) of the noise, a time constant of τ = 300 μs was set. For the estimation of LSD, we acquired the LIA signal for 1 minute with a sampling rate of s = 10 kHz and subsequently the LIA signal was Fast-Fourier transformed. The time constant of the LIA was set to τ = 1 ms for the construction of the LIA spectrum.

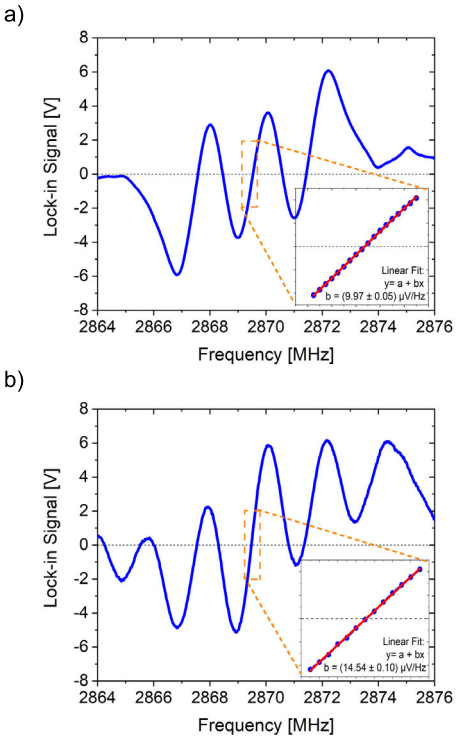

Figure 3 Lock-in spectrum with excitation of a single resonance (**a**) and simultaneous excitation of the three resonances separated by the hyperfine coupling (**b**). The insets shows the central linear zone and the value b of the slope the curve. b represents the figure of merit of the curve. The simultaneous excitation of the three resonances results in an improvement of b of a factor ≈ 1.5

3 Results

Figure 3(a) depicts the LIA signal in function of the microwave frequency. Three frequency ranges can be identified over which the LIA signal is directly proportional to the resonance shift and hence to the applied field. A yellow dashed rectangle encloses the central one. These three zones correspond to the three dips in the ODMR spectrum due to the hyperfine coupling of the NV electronic system with the ^{14}N nuclear spin. The LIA signal is linear in these zones because the LIA detection method is sensitive to the first derivative of the ODMR spectrum.

The figure of merit of the LIA detection method is represented by the slope b of the curve in the linear zone, as reported in Fig. 3(a). In this zone, δB_{NV} is related to the measured LIA signal S_{LIA} by [21]:

$$\delta B_{\mathrm{NV}} = \frac{h}{g\mu_B}\delta\nu_+ = \frac{h}{g\mu_B}\frac{1}{b}S_{\mathrm{LIA}}. \tag{2}$$

It is possible to increase the slope of the curve (and thus the sensitivity of the technique) by simultaneously addressing all the three resonances [21, 25]. To this scope, three frequency-modulated microwave tones separated by the hyperfine splitting $A_{\mathrm{orth}} = 2.16$ MHz were generated. When the center tone is at the frequency of the center resonance, all three resonance are excited, thus enhancing the slope of the curve. Figure 3(b) shows an example of the LIA spectrum for multiple frequency excitation. b is increased by a factor ≈ 2 compared to single-tone excitation.

The minimum detectable field B_{min} is

$$B_{\mathrm{min}} = \frac{h}{g\mu_B}\frac{1}{b}\frac{\sigma_S}{\sqrt{N}}, \tag{3}$$

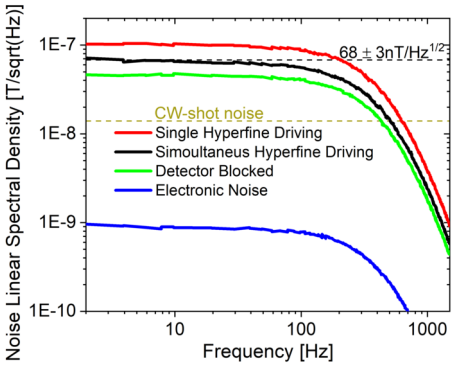

Figure 4 Comparison between the linear spectral densities (LSD) of the readout of the NV sensor in single hyperfine driving regime (red line) and in the simultaneous hyperfine driving (black line). The linear spectral density of the read-out with the detector blocked(green line), with the input of the LIA disconnected (blue line) and the Continous Wave(CW)-shot noise (dark green dashed line) are also shown. The value of the low-frequency plateau gives the magnetic sensitivity of the measurement. The simultaneous hyperfine driving improvement the sensitivity of a factor ≈ 1.5

where we have considered N independent measurements and that S_{LIA} is affected by an uncertainty equal to σ_S. Increasing the total time of measurement T leads to the usual scaling of the sensitivity η:

$$\eta = B_{\min}\sqrt{T} = \frac{h}{g\mu_B}\frac{1}{b}\frac{\sigma_S}{\sqrt{N}}\sqrt{T}, \tag{4}$$

Figure 4 shows the Linear Spectral Density of the LIA noise multiplied by the factor $\frac{g\mu_B h}{b}$, as defined in equation Eq. (3). For the Lock-in detection scheme described in this work, η corresponds to the low-frequency plateau in Fig. 4. This figure also shows the shot-noise limit for the single hyperfine driving, the Continuos Wave (CW) shot-noise limit being:

$$\eta_{\mathrm{CW}} = \frac{h}{g\mu_B}\frac{\sqrt{I_0}}{\max(\frac{\partial I_0}{\partial \nu})} \tag{5}$$

as results from ODMR spectrum:

$$\eta_{\mathrm{CW}} = K\frac{h}{g\mu_B}\frac{\Delta\nu}{2\sqrt{I_0}C} = 12.5\ \mathrm{nT/Hz^{1/2}}, \tag{6}$$

where $\Delta\nu = 1.072$ MHz is the linewidth, $C = 0.00273$ the contrast for the central dip of the hyperfine spectrum and $K = 0.31$ is a specific constant of this line. $I_0 = 3.03 \cdot 10^{10}\ \mathrm{s^{-1}}$ is estimated from the optical power incident onto the photodiode $W = 8.5$ nW, considering a photon energy $E_{\mathrm{ph}} = 2.84 \cdot 10^{-19}$ J.

Figure 4 shows that simultaneous driving improves the sensitivity by a factor of $\approx$1.5. This improvement is due to two contributions: (i) an increase in the slope b (ii) no significant increase in the LIA noise.

To point out the biocompatibility of this method, we measured the magnetic sensitivity for different applied powers, see Fig. 5. The sensitivity decreased by lowering the laser power. There is a tradeoff between laser power reduction that improves biocompatibility and sensitivity that will be discussed in detail in the next section. In the next section, we will discuss also which maximum power a biological system can bear.

4 Discussion

Our method is in principle able to resolve the contribution of a single cell to the magnetic field considering the fact that in our case the sensing volume is defined by the laser spot in x-y plane of $(10 \times 10)\ \mu\mathrm{m}^2$, and the thickness of NV-rich layer of 15 nm (along z-axis).

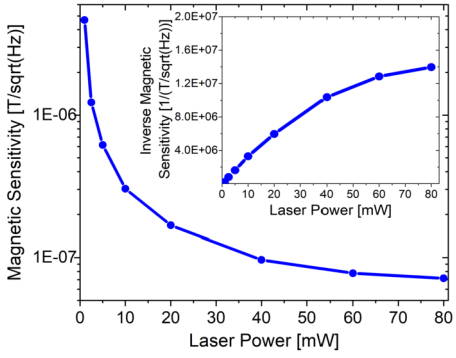

Figure 5 Magnetic Sensitivity for different values of the applied optical power. In the inset, the inverse of the sensitivity is shown for the same power values. Uncertainties are too small for being visible. The magnetic sensitivity improves increasing the applied optical power

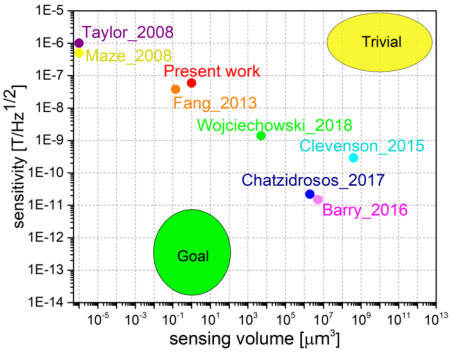

Figure 6 The sensitivity in function of the sensing volume for the present study and from data taken from literature [NV [31], ND 2008 [32], Fang 2013 [33], Barry 2016 [21], Wojciechowski 2018 [26], Clevenson 2015 [27], Chatzidrosos 2017 [28]]. The region of interest for biological application is defined by the green region

We obtained a sensitivity of $\eta = 68 \pm 3$ nT/$\sqrt{\text{Hz}}$ for an optical power of 80 mW: this value is beyond (or at least well comparable) with the one obtained in previous works if the sensing volume is taken in account [21, 26–28], see Fig. 6. Nonetheless, it has to be underlined that it is not proved that living cells can sustain 80 mW of power radiating on a surface of 100 μm^2, even considering that we apply this power only for a measurement time of 10 ms in a measurement cycle of 1 s. On the other hand, living neuronal cells can surely tolerate without being affected an optical power of 3 mW applied for minutes in the same optical geometry and similar applied microwave powers of our setup [13]. Considering that we apply the optical power only for few milliseconds, we can estimate a conservative biocompatible optical power $\geq$ 10 mW, that results in a sensitivity around $\eta_{\text{bio}} \leq 200$ nT/$\sqrt{\text{Hz}}$.

This value of sensitivity still needs to be increased to sense neuron (or hearth cells) activity, where we expect a magnetic field of 1-10 nT in proximity of a single channel (a functionalised nanodiamond can in principle be targeted at nanometric distance from the channel) or when considering tissue slices. Furthermore, ion channels clustering can further increase the previous values.

In order to achieve accurate magnetic sensing from biological samples at the (sub-)cellular scale, we envisage the following improvements as necessary: (i)use of pulsed techniques (ii) use of isotopically-purified samples (ii) protection of the sample from the laser heating. The pulsed techniques that should be implemented are Ramsey type measurements [29], this techinques as a better contrast compared to CW ODMR and allow to use a higher optical power. Isotopically purified samples would allow a higher concentration of NV with an extended coherence time T_2^*. An aluminum layer can protect the sample

from laser heating, as demonstrated in studies on macroscopic samples [21, 30], acting as well as reflective layer and heatsink. For cellular scale measurements, the thickness of the reflective layer should be reduced to a few micrometers, and the biocompatibility of the layer should be considered. Also, an appropriate optical geometry would increase the reflection at the sensor-sample interface, thus increasing the photoluminescence and decreasing the sample heating. For example, in [30] the green laser is polarized beam and incident at the Brewster angle, while in [21] the laser beam is incident at a grazing angle.

Barry et al. [21] estimated that pulsed sequences and new techniques in sample preparation would allow a 300-fold improvement in the sensitivity. Considering this improvement, and taking into account a sensitivity of $\eta_{\mathrm{bio}} \leq 200\ \mathrm{nT}/\sqrt{\mathrm{Hz}}$ at an optical power of 10 mW, a five-fold sensitivity improvement is still needed to achieve the magnetic sensing of the heart activity or neuronal cells. The above-listed methods for protection from heating stated above could allow the adoption of higher optical powers and thus reaching the desired sensitivity.

5 Conclusions

We presented an experimental ODMR apparatus and sensing protocol compatible with the measurement of magnetic fields in biological systems at an intracellular/cellular scale, and with a sensitivity beyond or at least comparable to previous works when sensing volume is considered. These results (point out) a clear strategy for magnetic sensing at cellular level, contributing to paving the way to practical biological applications of these methods. Neverthless, it must be emphasized that due to the small, potentially at nanoscale, volume of our technique, this can find a broad application, beyond the biological example that we have discussed.

Acknowledgements
The authors wish to thank Elio Bertacco for the technical help in implementing the frequency modulation and Giulia Tomagra for the interesting discussions about the biocompatibility of the setup.

Funding
This work has received funding from the European Commision's PATHOS EU H2020 FET-OPEN grant no. 828946 and Horizon 2020, from the EMPIR Participating States in the context of the projects EMPIR-17FUN06 "SIQUST" and 17FUN01 "BeCOMe", from the project Piemonte Quantum Enabling Technologies (PiQuET) funded by the Piemonte Region, from the Coordinated Research Project F11020 of the International Atomic Energy Agency (IAEA), from the Departments of Excellence Project (L. 232/2016), funded by MIUR, from National Collaborative Research Infrastructure Strategy (NCRIS) programme funding by the Australian Government-Department of Education, Skill and Employment, and from the project Finanziamento ex-post di progetti di ricerca di Ateneo of the University of Torino (funded by Compagnia di SanPaolo Foundation).

Abbreviations
AOM, Acousto Optical Modulator; CW, Continuos Wave; LIA, Lock-In Amplifier; LSD, Linear Spectral Density; NV, Nitrogen-Vacancy; ODMR, Optically Detected Magnetic Resonance; PL, Photoluminescence; SPD, Single-Photon Detector; SQUID, Superconductive Quantum Interference Device.

Availability of data and materials
All the experimental data presented are available from the authors upon reasonable request.

Competing interests
The authors declare that they have no competing interests.

Authors' contributions
EB, EM, PT, GP developed the experimental system and performed the experiments in INRIM laboratories, directed by MG, EB and GP, analysed the results. SDT, JF, FP, and ŽP prepared the samples. PO, IPD and MG supervised the project. All authors contributed to writing the manuscript. All authors read and approved the final manuscript.

Author details
[1]Istituto Nazionale di Ricerca Metrologica, Strada delle cacce 91, Turin, Italy. [2]Physics Department and NIS Centre of Excellence, University of Torino, Turin, Italy. [3]Istituto Nazionale di Fisica Nucleare (INFN) Sez. Torino, Turin, Italy. [4]Centre for Accelerator Science, Australian Nuclear Science and Technology Organisation, New Illawarra rd., Lucas Heights, Australia.

Publisher's Note

Received: 18 June 2020 Accepted: 7 October 2020 Published online: 21 October 2020

References

1. Petrini G, Moreva E, Bernardi E, Traina P, Tomagra G, Carabelli V, Degiovanni IP, Genovese M. Is a quantum biosensing revolution approaching? Perspectives in NV-assisted current and thermal biosensing in living cells. Adv Quantum Technol. 2020;2000066. https://doi.org/10.1002/qute.202000066.
2. Xiong J, Fox PT, Gao J-H. Directly mapping magnetic field effects of neuronal activity by magnetic resonance imaging. Hum Brain Mapp. 2003;20(1):41–9.
3. Li B, Virtanen JP, Oeltermann A, Schwarz C, Giese MA, Ziemann U, Benali A. Lifting the veil on the dynamics of neuronal activities evoked by transcranial magnetic stimulation. eLife. 2017;6:30552.
4. Kullmann DM. Neurological channelopathies. Annu Rev Neurosci. 2010;33:151–72.
5. Waxman SG. Axonal conduction and injury in multiple sclerosis: the role of sodium channels. Nat Rev Neurosci. 2006;7(12):932–41.
6. Tomagra G, Picollo F, Battiato A, Picconi B, De Marchis S, Pasquarelli A, Olivero P, Marcantoni A, Calabresi P, Carbone E, et al. Quantal release of dopamine and action potential firing detected in midbrain neurons by multifunctional diamond-based microarrays. Front Neurosci. 2019;**13**.
7. Cohen D. Magnetic fields around the torso: production by electrical activity of the human heart. Science. 1967;156(3775):652–4.
8. Wacker-Gussmann A, Strasburger JF, Cuneo BF, Wakai RT. Diagnosis and treatment of fetal arrhythmia. Am J Perinatol. 2014;31(07):617–28.
9. Faley M, Poppe U, Urban K, Paulson D, Fagaly R. A new generation of the hts multilayer dc-squid magnetometers and gradiometers. Journal of physics: conference series. vol. 43. Bristol: IOP Publishing; 2006.
10. Baudenbacher F, Fong L, Holzer J, Radparvar M. Monolithic low-transition-temperature superconducting magnetometers for high resolution imaging magnetic fields of room temperature samples. Appl Phys Lett. 2003;82(20):3487–9.
11. Yu S-J, Kang M-W, Chang H-C, Chen K-M, Yu Y-C. Bright fluorescent nanodiamonds: no photobleaching and low cytotoxicity. J Am Chem Soc. 2005;127(50):17604–5.
12. Zhu Y, Li J, Li W, Zhang Y, Yang X, Chen N, Sun Y, Zhao Y, Fan C, Huang Q. The biocompatibility of nanodiamonds and their application in drug delivery systems. Theranostics. 2012;2(3):302.
13. Guarina L, Calorio C, Gavello D, Moreva E, Traina P, Battiato A, Tchernij SD, Forneris J, Gai M, Picollo F et al. Nanodiamonds-induced effects on neuronal firing of mouse hippocampal microcircuits. Sci Rep. 2018;8(1):1–14.
14. Schrand AM, Huang H, Carlson C, Schlager JJ, Ōsawa E, Hussain SM, Dai L. Are diamond nanoparticles cytotoxic?. J Phys Chem B. 2007;111(1):2–7.
15. Liu K-K, Cheng C-L, Chang C-C, Chao J-I. Biocompatible and detectable carboxylated nanodiamond on human cell. Nanotechnology. 2007;18(32):325102.
16. Gruber A, Dräbenstedt A, Tietz C, Fleury L, Wrachtrup J, Von Borczyskowski C. Scanning confocal optical microscopy and magnetic resonance on single defect centers. Science. 1997;276(5321):2012–4.
17. Neumann P, Beck J, Steiner M, Rempp F, Fedder H, Hemmer PR, Wrachtrup J, Jelezko F. Single-shot readout of a single nuclear spin. Science. 2010;329(5991):542–4.
18. Robledo L, Childress L, Bernien H, Hensen B, Alkemade PF, Hanson R. High-fidelity projective read-out of a solid-state spin quantum register. Nature. 2011;477(7366):574–8.
19. Childress L, Dutt MG, Taylor J, Zibrov A, Jelezko F, Wrachtrup J, Hemmer P, Lukin M. Coherent dynamics of coupled electron and nuclear spin qubits in diamond. Science. 2006;314(5797):281–5.
20. Rondin L, Tetienne J-P, Hingant T, Roch J-F, Maletinsky P, Jacques V. Magnetometry with nitrogen-vacancy defects in diamond. Rep Prog Phys. 2014;77(5):056503.
21. Barry JF, Turner MJ, Schloss JM, Glenn DR, Song Y, Lukin MD, Park H, Walsworth RL. Optical magnetic detection of single-neuron action potentials using quantum defects in diamond. Proc Natl Acad Sci. 2016;113(49):14133–8.
22. McNally HA, Rajwa B, Sturgis J, Robinson JP. Comparative three-dimensional imaging of living neurons with confocal and atomic force microscopy. J Neurosci Methods. 2005;142(2):177–84.
23. Schoenfeld RS, Harneit W. Real time magnetic field sensing and imaging using a single spin in diamond. Phys Rev Lett. 2011;106(3):030802.
24. Sasaki K, Monnai Y, Saijo S, Fujita R, Watanabe H, Ishi-Hayase J, Itoh KM, Abe E. Broadband, large-area microwave antenna for optically detected magnetic resonance of nitrogen-vacancy centers in diamond. Rev Sci Instrum. 2016;87(5):053904.
25. El-Ella HA, Ahmadi S, Wojciechowski AM, Huck A, Andersen UL. Optimised frequency modulation for continuous-wave optical magnetic resonance sensing using nitrogen-vacancy ensembles. Opt Express. 2017;25(13):14809–21.
26. Wojciechowski AM, Karadas M, Osterkamp C, Jankuhn S, Meijer J, Jelezko F, Huck A, Andersen UL. Precision temperature sensing in the presence of magnetic field noise and vice-versa using nitrogen-vacancy centers in diamond. Appl Phys Lett. 2018;113(1):013502.
27. Clevenson H, Trusheim ME, Teale C, Schröder T, Braje D, Englund D. Broadband magnetometry and temperature sensing with a light-trapping diamond waveguide. Nat Phys. 2015;11(5):393–7.
28. Chatzidrosos G, Wickenbrock A, Bougas L, Leefer N, Wu T, Jensen K, Dumeige Y, Budker D. Miniature cavity-enhanced diamond magnetometer. Phys Rev Appl. 2017;8(4):044019.
29. Barry JF, Schloss JM, Bauch E, Turner MJ, Hart CA, Pham LM, Walsworth RL. Sensitivity optimization for nv-diamond magnetometry. Rev Mod Phys. 2020;92(1):015004.
30. Webb JL, Troise L, Hansen NW, Olsson C, Wojciechowski A, Achard J, Brinza O, Staacke R, Kieschnick M, Meijer J, et al. Detection of biological signals from a live mammalian muscle using a diamond quantum sensor. 2020. arXiv preprint. arXiv:2008.01002.

31. Taylor J, Cappellaro P, Childress L, Jiang L, Budker D, Hemmer P, Yacoby A, Walsworth R, Lukin M. High-sensitivity diamond magnetometer with nanoscale resolution. Nat Phys. 2008;4(10):810–6.
32. Maze JR, Stanwix PL, Hodges JS, Hong S, Taylor JM, Cappellaro P, Jiang L, Dutt MG, Togan E, Zibrov A et al. Nanoscale magnetic sensing with an individual electronic spin in diamond. Nature. 2008;455(7213):644–7.
33. Fang K, Acosta VM, Santori C, Huang Z, Itoh KM, Watanabe H, Shikata S, Beausoleil RG. High-sensitivity magnetometry based on quantum beats in diamond nitrogen-vacancy centers. Phys Rev Lett. 2013;110(13):130802.